Evidence of antimagnetic rotation in ^{100}Pd

S. Sihotra,[1,*] D. Kumar,[1] M. Kaur,[1] V. Singh,[1] S. Saha,[2] J. Sethi,[2] R. Palit,[2] N. Singh,[1] and D. Mehta[1]

[1]*Department of Physics, Panjab University, Chandigarh 160014, India*

[2]*Department of Nuclear and Atomic Physics, Tata Institute of Fundamental Research, Mumbai 400005, India*

(Received 19 May 2020; accepted 28 August 2020; published 16 September 2020)

Lifetimes of states in a negative-parity band involving the $\nu h_{11/2}$ orbital in ^{100}Pd have been determined through Doppler shift attenuation method (DSAM) measurements performed using Indian National Gamma Array (INGA) spectrometer. The measured quadrupole transition rates, $B(E2)$, exhibit a decreasing behavior with increasing angular momentum and with large observed $\Im^{(2)}/B(E2)$ values. The experimental observations and semiclassical particle-rotor model calculations favor the antimagnetic rotation (AMR) phenomenon based on the $\pi(g_{9/2})^{-4} \otimes \nu[h_{11/2}\,(g_{7/2})^3]$ configuration for the negative-parity band in the ^{100}Pd isotope.

DOI: 10.1103/PhysRevC.102.034321

I. INTRODUCTION

Antimagnetic geometric structure in a nucleus consists of twin shears, with two proton blades symmetrically coupled to a neutron blade. This geometry retains the $R_z(\pi)$ symmetry, and weak $E2$ transitions are observed due to small deformation. The protons are coupled in a way such that the perpendicular components of the magnetic moments, $\mu_\perp$, exactly cancel each other. Thus, dipole transitions ($M1$) are not observed and the energy levels in the band are connected by weak $E2$ transitions reflecting a nearly spherical core. Anisotropy in the current distribution due to the presence of a few high spin particles and holes outside the nearly spherical core is responsible for antimagnetic rotation (AMR) within the framework of the shears mechanism [1–3]. The shears mechanism is prevalent in nuclei in the mass $A \approx 100$ region due to the presence of valance particles and holes in the vicinity of the $N = 50$ shell closure. In this scenario, the coupling for this mass region is such that two pairs of stretched $\pi g_{9/2}$ holes point in opposite directions and gradually align along the direction of the stretched $h_{11/2}$ neutrons. Another similar phenomenon has been interpreted as smoothly terminating bands of regular bandlike structure with different characteristic features where the similar decreasing trend of $B(E2)$ values was observed for several nuclei. These bands show the characteristic of gradually decreasing dynamic moments of inertia with increasing spin in contrast to a fairly constant dynamic moment of inertia (without any collective contribution) in the case of AMR. To date, observations of AMR bands have been reported in many weakly deformed Cd and Pd nuclei in the $A \approx 100$ region. On the basis of lifetime measurements, AMR bands based on different configurations have been observed in $^{105-108,110}$Cd [4–10] and ^{101,104}Pd [11,12]. Similarly, possible AMR bands have been reported in ^{142,143}Eu [13,14]. The observed slower fall of $B(E2)$ values in ^{110}Cd as compared to those observed in pure AMR bands in the ^{106,108}Cd isotopes evidences an interplay between antimagnetic and core rotation [10]. The fall of $B(E2)$ values in ^{105}Cd [4,15] was explained within the framework of tilted axis cranking based on covariant density functional theory with polarization effects, and this framework also supports the two-shears-like mechanism in AMR.

The present work focuses on new experimental data obtained for the excited states of ^{100}Pd. Prior to this work, high-spin states in this nucleus were investigated successively by Perez *et al.* [16] and Zhu *et al.* [17], and level structures up to $E_x \approx 16$ MeV excitation energy and spin $I \approx 25\hbar$ were reported. Perez *et al.* [16] reported maximal spin alignment states in various band structures on the basis of cranked Strutinsky-type total Routhian surface calculations. Also, possible evidence for the existence of octupole correlations in ^{100}Pd is discussed. Zhu *et al.* [17] provided evidence of AMR for a rotational-band-like cascade of transitions in the yrast negative-parity band in ^{100}Pd on the basis of (i) the small deformation associated with these transitions, as evidenced by very limited lifetime information estimated from the experiment, and (ii) very large estimated $\Im^{(2)}/B(E2)$ ratios in the range of 230–1120 $\hbar^2\text{MeV}^{-1}(e\text{b})^{-2}$. The results were in agreement with expectations from theoretical results, and angular momentum in this band is proposed to be mainly generated by "bending " the side prongs, formed by the pairs of stretched $\pi g_{9/2}$ holes, along the axis of rotation. The work clearly demands a full Doppler shift attenuation method (DSAM) measurement of lifetimes for the yrast negative-parity band to confirm the novel AMR phenomenon. In the present work, the level lifetimes have been measured for the yrast negative-parity band of ^{100}Pd by DSAM [18] using an advanced array of Compton-suppressed clover detectors [19]. The present experimental results are discussed in the framework of semiclassical particle-rotor model [10] to support the AMR phenomenon. Preliminary reports on the present studies have been reported earlier [20].

*Corresponding author: ssihotra@pu.ac.in

II. EXPERIMENTAL DETAILS

High spin states of the ^{100}Pd nucleus were populated in the ^{75}As(^{31}P, $2p4n$) ^{100}Pd fusion-evaporation reaction at $E_{\rm lab} = 125$ MeV. The deexcitations were investigated through in-beam γ-ray spectroscopic techniques. The ^{31}P beam was delivered by the Pelletron-LINAC facility at Tata Institute of Fundamental Research (TIFR), Mumbai. The ^{75}As target of thickness 2.8 mg/cm^2 was prepared by vacuum evaporation and rolled onto a 10 mg/cm^2 thick Pb backing. The recoiling nuclei had a maximum initial velocity of $v_o/c = 2.7\%$, in the target. The recoiling nuclei in the excited states were stopped within the target and the deexciting γ rays were detected using the Indian National Gamma Array (INGA) [19] consisting of 21 Compton suppressed clover detectors. In the present work, the array consisted of two detectors at 23°, three detectors each at 40°, 65°, 115°, 140°, and 157°, and four detectors at 90° with respect to the beam axis. Two- and higher-fold clover coincidence events were recorded in a fast digital data acquisition system based on Pixie-16 modules of XIA LLC [21]. About 1.1×10^{10} γ-γ and 3.2×10^{8} γ-γ-γ events were collected in the experiment. The ^{106}Cd compound nucleus produced in the present experiment decays via several reaction channels [22]. It is worth mentioning that data from the same experiment with backed target were also used for establishing level schemes and measuring the subpicosecond lifetimes using the Doppler shift attenuation method (DSAM) [18] in ^{101}Pd [11,22] and ^{102}Ag [23] nuclei.

III. DATA ANALYSIS AND RESULTS

The data were sorted using "Multi pARameter time stamped based COincidence Search program" (MARCOS) [21], developed at TIFR, that sorts the time-stamped data to generate E_γ-E_γ matrices and E_γ-E_γ-E_γ cubes compatible with RADWARE format [24]. The E_γ-E_γ matrices [22,23] were also generated for the directional correlations of oriented state (DCO) analysis [25]. The integrated polarization directional correlation from oriented nuclei (IPDCO) analysis [26] was performed using two asymmetric polarization matrices corresponding to the parallel and perpendicular segments (with respect to the emission plane) of the clover detector chosen as a Compton polarimeter along one axis and the coincident γ rays in all the detectors along the other axis.

Double-gated analysis using the cube was performed to establish the level scheme of ^{100}Pd. A partial level scheme of ^{100}Pd containing a quadrupole cascade of γ rays of the yrast negative-parity band is shown in Fig. 1. It preserves general features based on the γ-ray coincidence relationships in the previously established schemes [16,17]. The negative-parity band comprises mainly the $\Delta I = 2$ quadrupole transitions and is built on the $I^\pi = 9^-$ level. In the present work this quadrupole cascade is confirmed up to $I^\pi = 25^{(-)}$ level. Multifragmentation at higher spin states and doppler energy smearing of the γ-ray peaks constrain further placement of transitions in the negative-parity band. A spectrum obtained by adding various double-gated spectra in the negative-parity band is shown in Fig. 2. The DCO and IPDCO [26] ratio values along with the assigned multipolarities for negative-parity

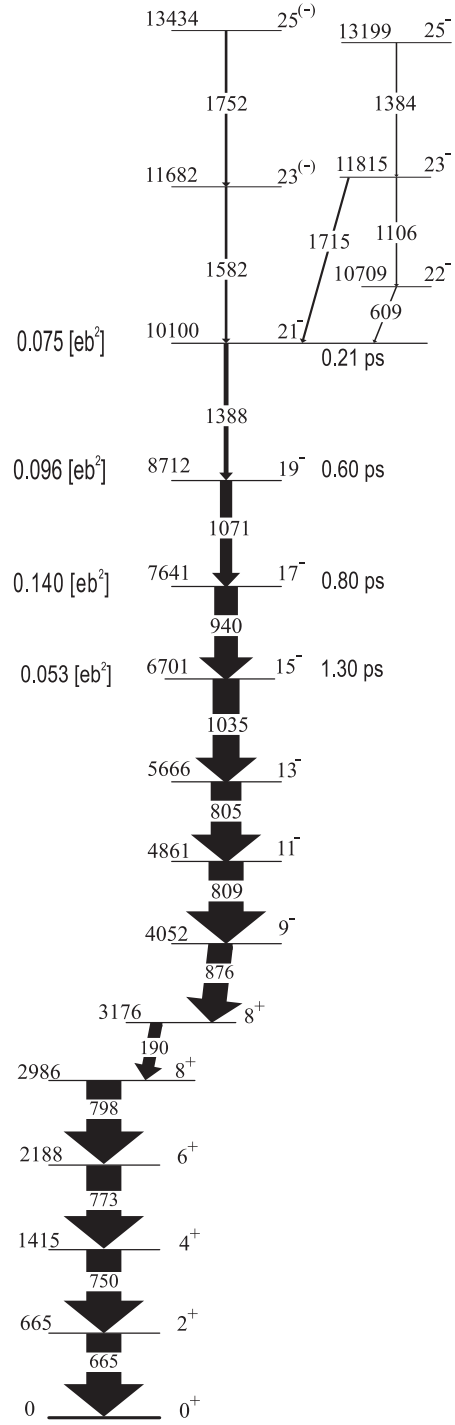

FIG. 1. Partial level scheme of ^{100}Pd of present interest. Energies of γ rays and levels are given in keV. The width of the arrows is proportional to the relative γ-ray intensity. Lifetimes of states are given on the right-hand side and the $B(E2)$ values are given on the left-hand side.

band transitions are found to be consistent with the previous work [16]. In the present work, the parity of the 3176 kev level is confirmed on the basis of IPDCO measurements as $I^\pi = 8^+$, which is also proposed by Perez *et al.* [16].

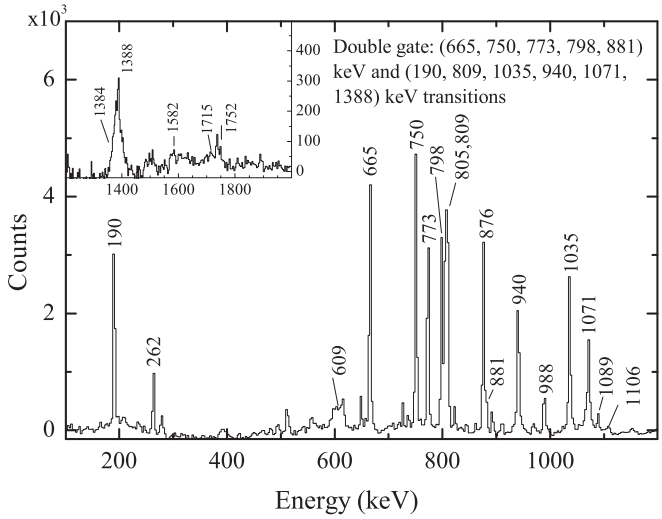

FIG. 2. The double-gated γ-ray coincidence spectra showing the transitions of the negative-parity band. The spectra are generated with coincidence gates from a list of 665, 750, 773, 798, and 881 keV transitions and 190, 809, 1035, 940, 1071, and 1388 keV transitions. The inset shows high energy transitions of the band. The unmarked peaks are contaminations.

The data from the present experiment involving ^{75}As target with backing was used for lifetime measurements of states in the yrast negative-parity band in ^{100}Pd (Fig. 1) using the DSAM [18]. The γ-γ coincidence events were sorted using MARCOS program [21] into three asymmetric matrices with the x axes corresponding to γ rays in the respective detectors at 140°, 90°, and 40°, while the y axes correspond to γ rays in the detectors at any other position. The LINESHAPE program [18] was used for fitting the line shapes of γ rays detected at 40° and 140°. The program takes into account energy loss of the ^{31}P beam through the ^{75}As target, and energy loss and angular straggling of recoils through the ^{75}As target and the Pb backing. Shell-corrected Northcliffe and Schilling stopping powers [27] were used for energy loss calculations. The value of time step and the number of recoil histories were 0.01 ps and 5000, respectively. The best fit was obtained through the least-square minimization procedures SEEK, SIMPLEX, and MIGRAD [18]. The lifetimes of states in the negative-parity band were deduced from the global fit of the cascade of γ rays, where only the in-band and side-feeding lifetimes were allowed to vary. Further, the 90° spectra were also included in line-shape analysis to check for contamination peaks. In the fitting procedure, the side-feeding into each level of the band was considered as a cascade of five transitions having a fixed moment of inertia comparable to that of the in-band sequences. The line-shape analysis was carried out step by step, starting at the 21^- level at 10 100 keV. The lifetimes of states with $15\hbar \leqslant I \leqslant 21\hbar$ in ^{100}Pd were deduced by performing line-shape analysis of the respective depopulating transitions in the coincidence spectra generated using the standard gate on transition below (GTB) procedure [28]. The line shapes of higher transitions were obtained by gating the 809 keV ($11^- \rightarrow 9^-$) transition, which is below the transitions of interest.

In the present experiment, a number of transitions populated in ^{100,101,102}Pd isotopes are overlapping [11]. The transition gate selection and line-shape analysis of the respective depopulating transitions were carefully performed. The line shapes for 809 keV ($11^- \rightarrow 9^-$) and 805 keV ($13^- \rightarrow 11^-$) were found to overlap in the lower gates. The lifetimes of higher-lying 11 682 keV ($23^{(-)}$) and 13 434 keV ($25^{(-)}$) levels could not be determined, because of weak intensity of the 1582 keV ($23^- \rightarrow 21^-$) and 1752 keV ($25^- \rightarrow 23^-$) γ transitions. The effective lifetime of the 21^- state was determined to be 0.21 ps from line-shape analysis of the 1388 keV transition in the 809 keV ($11^- \rightarrow 9^-$) and 805 keV ($13^- \rightarrow 11^-$) transition-gated spectra by assuming 100% side-feeding for this level. By fixing the lifetime of the 21^- state (0.21 ps), the lifetimes of lower levels have been deduced in the broad gate on the 809 keV ($11^- \rightarrow 9^-$) transition. The lifetimes of 19^-, 17^-, and 15^- states were determined from a global fit of line shapes of the respective depopulating 1071, 940, and 1035 keV γ transitions. All the results were thoroughly confirmed by varying the 809 keV transition gate limits. The obtained line shapes of these transitions are shown in Figs. 3 and 4. The uncertainties in the lifetimes were obtained by using the MINOS routine [29]. The mean lifetimes and statistical uncertainties obtained from the line-shape analysis are given in Table I. The errors given in Table I do not account for additional systematic uncertainties, which may be as large as ±20% and arise from the choice of stopping powers used in the analysis. In the earlier investigations on ^{100}Pd using a ^{72}Ge target with backing and a ^{35}Cl beam, Zhu *et al.* [17] made an attempt to estimate the lifetimes of the states depopulated by 1071 and 1388 keV γ transitions. A novel difference spectrum, obtained by subtracting the gated spectrum from the backward detectors from that corresponding to the forward detectors, was used for this purpose. The lifetime values were assessed to range between ≈0.3 ps and ≈1.0 ps, which enfolds the present measured values.

IV. DISCUSSION

The $B(E2)$ transition rates in units of $(eb)^2$ were extracted from the present measured lifetime values by using the formula

$$B(E2) = \frac{0.0816\, B_\gamma}{E_\gamma^5\, \tau\, [1 + \alpha_t(E2)]}\ [(eb)^2], \qquad (1)$$

where E_γ is the energy of a pure E2 transition in MeV, τ is the level lifetime in picoseconds, and α_t is the total internal conversion coefficient for the γ transition. The extracted $B(E2)$ values are given in Table I and also plotted as a function of angular momentum in Fig. 5(a). The plot shows a decreasing behavior in the higher-spin portion. The dynamic moment of intertia ($\Im^{(2)}$) and $\Im^{(2)}/B(E2)$ values deduced from the present experimental data of the negative-parity band in ^{100}Pd are plotted as a function of spin in Figs. 5(b) and 5(c), respectively. These values are also given in Table I. $\Im^{(2)}/B(E2)$ values of ^{104}Pd [12] are also plotted in Fig. 5(c) for comparison. The falling trend of $B(E2)$ and large $\Im^{(2)}/B(E2)$ values in the spin range $17\hbar \leqslant I \leqslant 21\hbar$ suggest AMR in the higher-spin portion of this band [Figs. 5(b) and 5(c)].

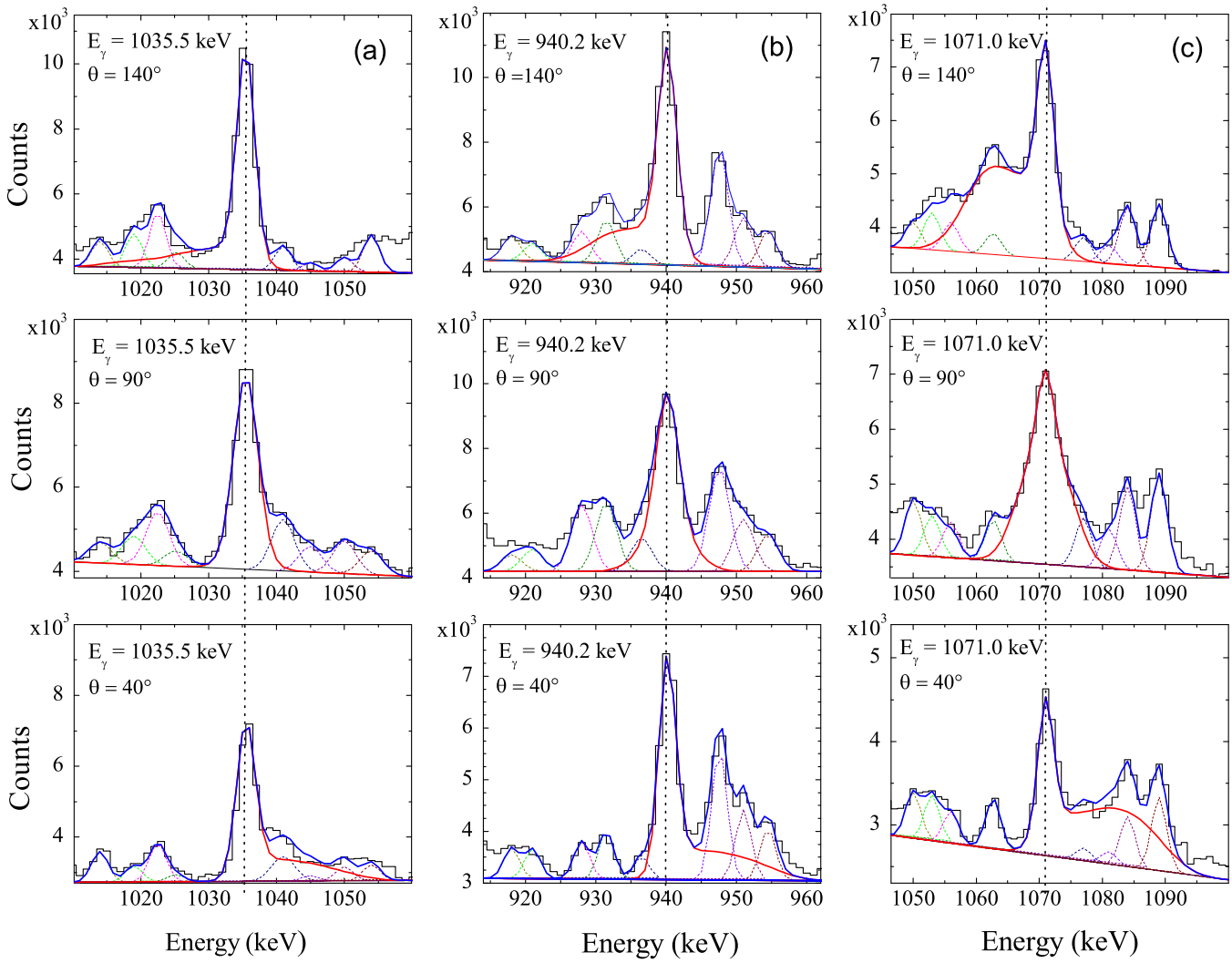

FIG. 3. The line-shape fits for (a) 1035.5 ($15^- \rightarrow 13^-$) keV, (b) 940.2 ($17^- \rightarrow 15^-$) keV, (c) 1071.0 ($19^- \rightarrow 17^-$) keV transitions in the 809 keV transition-gated spectra at 140°, 90°, and 40° with respect to the beam direction.

In present work, we address the AMR character of the negative-parity band in ^{100}Pd within the framework of the semiclassical particle-rotor model (SCM) [2,10,30–32]. In this model the total energy is the sum of the rotational energy of the core and the effective interaction $V_2P_2(\theta)$ between the high-j protons and high-j neutron holes. The total energy is expressed as

$$E(I) = \frac{(I - j_\pi - j_\nu)^2}{2\Im} + \frac{V_{\pi\nu}}{2}\left(\frac{3\cos^2\theta - 1}{2}\right) + \frac{V_{\pi\nu}}{2}\left(\frac{3\cos^2(-\theta) - 1}{2}\right) - \frac{V_{\pi\pi}}{n}\left(\frac{3\cos^2(2\theta) - 3}{2}\right), \tag{2}$$

where the first term represents the rotational contribution and its associated moment of inertia. The second and third terms represent the repulsive interaction between the neutron particles and the proton holes, respectively and $V_{\pi\nu}$ is the interaction strength. The fourth term signifies the proton-proton (hole-hole) attractive interaction and has been assumed to be of the same form, with the additional boundary condition that it vanishes for $\theta = 0°$. This condition also implies that the attractive particle-particle interaction is absent. There is a scaling factor n between $V_{\pi\nu}$ and $V_{\pi\pi}$, determined by the actual number of particle-hole pairs for a single-particle configuration. The angular momentum generated by the interplay between collective rotation and AMR can be calculated by imposing the energy minimization condition as a function of θ on Eq. (2), which gives

$$I = aj + 2j\cos\theta + \frac{1.5\Im V_{\pi\nu}\cos\theta}{j} - \frac{6\Im V_{\pi\pi}\cos 2\theta\cos\theta}{nj}, \tag{3}$$

$$I = I_{\rm sh} + \Im\omega_{\rm sh}, \tag{4}$$

where $j = j_\pi$ and $a = j_\nu/j_\pi$. $I_{\rm sh}$ is the total angular momentum generated by the shears mechanism and represented by the first two terms of Eq. (3). $\Im\omega_{\rm sh}$ represents interplay between the shears mechanism and collective rotation and is represented by the last two terms of Eq. (3). $\omega_{\rm sh} = (\frac{dE_{\rm sh}}{d\theta})/(\frac{dI_{\rm sh}}{d\theta})$ represents the frequency associated with the

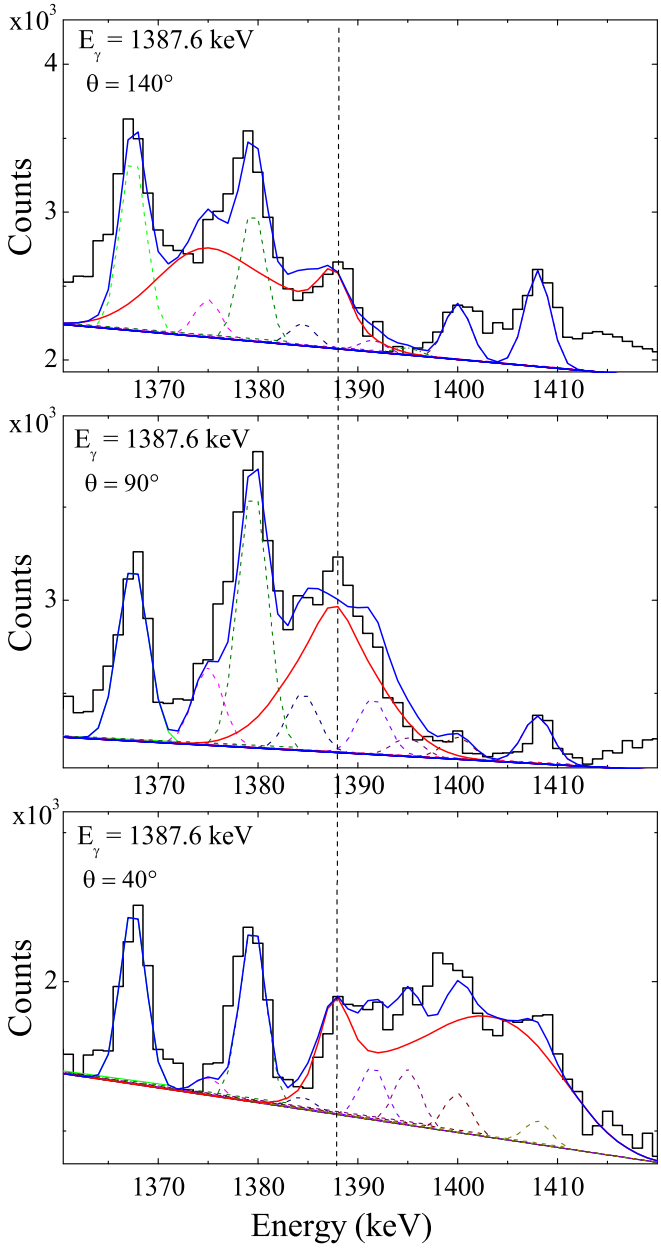

FIG. 4. The line-shape fits for the 1387.6 ($21^- \rightarrow 19^-$) keV transition in the 809 keV transition-gated spectra at 140°, 90°, and 40° with respect to the beam direction.

shears mechanism. The magnitude of $\Im$ can be estimated from the equation

$$\Im\omega_{\rm sh}|_{(\theta=0^\circ)} = I_{\rm max} - I_{\rm sh}^{\rm max}, \tag{5}$$

where $I_{\rm max}$ is the highest observed angular momentum state and $I_{\rm sh}^{\rm max}$ is the maximum angular momentum generated by the full closure of the double shears. A pictorial representation of the angular momentum generated by rotation and closing of the symmetric shears is given in previous work [11]. The rotational frequency is given by $\omega = \omega_{\rm cr} - \omega_{\rm sh}$, where $\omega_{\rm cr} = \frac{1}{2\Im_{\rm cr}}(2I+1)$ is the core rotational frequency and $\Im_{\rm cr}$ is the core moment of inertia, whose value can be estimated from the slope of the $I(\omega)$ plot for the band (before the neutron alignment). Thus, the model parameters for ^{100}Pd can be fixed from the experimental data or the systematics of the mass region [31].

TABLE I. Mean lifetime (τ) of the levels (I^π) deexcited by a γ ray of energy E_γ in ^{100}Pd. $B(E2)$ is the corresponding reduced transition probability.

$E\gamma$ (keV)	$I_f \rightarrow I_i$ ($\hbar$)	τ (ps)	$B(E2)$ $(e\text{b})^2$
1035	$15^- \rightarrow 13^-$	1.30(14)	0.053(15)
940	$17^- \rightarrow 15^-$	0.80(10)	0.140(7)
1071	$19^- \rightarrow 17^-$	0.60(7)	0.096(8)
1388	$21^- \rightarrow 19^-$	0.21[a]	0.075[a]

[a]Corresponds to the effective lifetime measurement assuming 100% side feeding.

The $B(E2)$ values have been calculated following the equation

$$B(E2) = \frac{15}{32\pi}(eQ_{\rm eff})^2 \sin^4\theta, \tag{6}$$

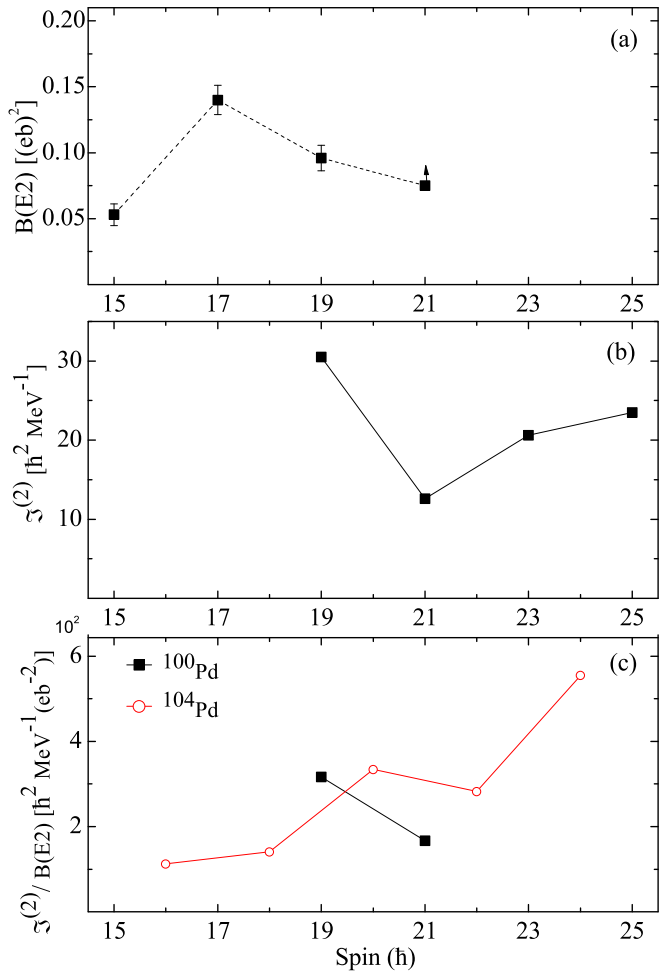

FIG. 5. (a) The experimental $B(E2)$ rates, (b) the dynamic moment of interia $\Im^{(2)}$, and (c) $\Im^{(2)}/B(E2)$ vs spin plots in the $\nu h_{11/2}$ band in ^{100}Pd and compared with ^{104}Pd [12].

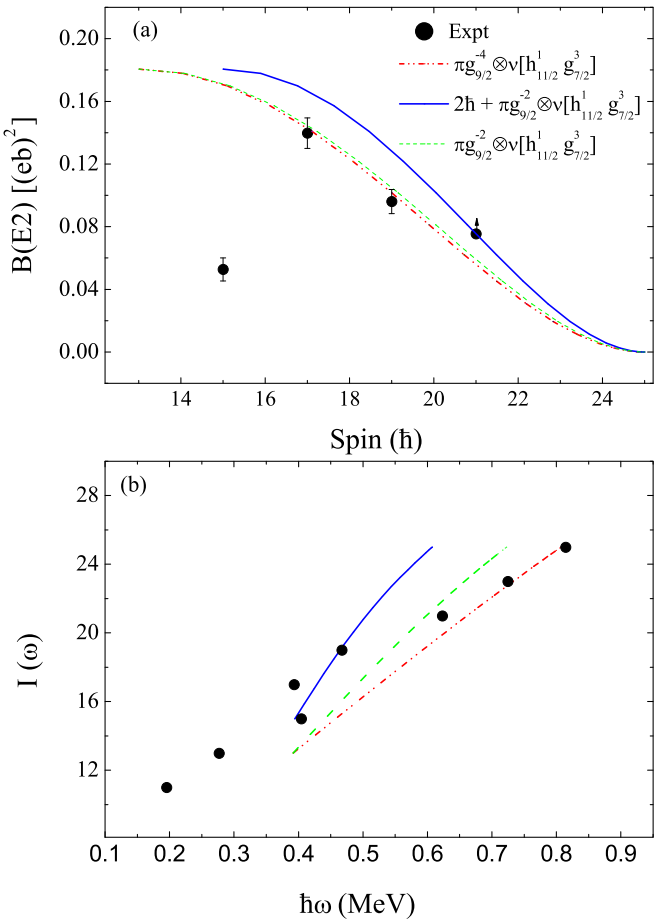

FIG. 6. The observed (a) $B(E2)$ rates and (b) $I(\omega)$ plots in ^{100}Pd. The line represents numerical values obtained from the semiclassical particle rotor model for the parameter set as given in the text.

where $eQ_{\rm eff} \approx 1.1\ e$b can be used for all the Pd isotopes since they have similar deformation and the value of $eQ_{\rm eff}$ is almost solely determined by the two proton holes [8]. The shears angle θ is determined from Eq. (2) for a given angular momentum state. Plots of $B(E2)$ vs spin and spin $I(\omega)$ vs frequency ($\hbar\omega$) obtained from the semiclassical model are compared with the experimental data in Figs. 6(a) and 6(b). Overall, the calculations reproduce the nature of the experimentally measured values very well.

In the present work, calculations were performed for two configurations for the investigation of AMR in this band. In the $\pi(g_{9/2})^{-2} \otimes \nu[h_{11/2}(g_{7/2})^3]$ configuration, at the bandhead state, the two $(g_{9/2})^{-1}$ proton blades are opposite to each other in the twin-shears structure. These systematic studies of AMR bands [10,12,31] suggest the $V_{\pi\nu}$ and $V_{\pi\pi}$ to be 1.2 MeV and 0.15–0.20 MeV, respectively, and similar interaction strengths are expected for ^{100}Pd. The other parameters of the semiclassical particle-rotor model for ^{100}Pd are deduced from the present experimental data and the systematics of the mass $A \approx 100$–110 region [10,12,31]. For the $\pi(g_{9/2})^{-2} \otimes \nu[h_{11/2}(g_{7/2})^3]$ configuration, the symmetric shears are formed between $j_\pi = 4.5\hbar$ and $j_\nu = 13\hbar$. For four neutron particles and two proton holes, there are eight possible particle-hole pairs, which implies $n = 8$. The shears parameters used were $j = 4.5\hbar$, $a = 2.89$, $V_{\pi\nu} = 1.2$ MeV, and $V_{\pi\pi} = 0.15$ MeV. For the negative-parity band with the configuration under consideration, $I_{\rm sh}^{\rm max} = 22\hbar$, $I_{\rm max} = 25\hbar$, and $\Im = 8\,\hbar^2{\rm MeV}^{-1}$. The bandhead frequency is $\hbar\omega \approx 0.402$ MeV at $I = 17\hbar$. $\Im$ was estimated using these values in Eq. (5) and $\Im_c$ was estimated to be $17\,\hbar^2{\rm MeV}^{-1}$ using the slope of the $I(\omega)$ plot [Fig. 6(b)] for the band before the neutron alignment. Figures 6(a) and 6(b) show comparisons between the theoretical and experimental $B(E2)$ values vs spin and spin vs frequency $I(\omega)$ plots, where the calculated frequencies have been shifted by the experimental bandhead frequencies. Further semiclassical particle-rotor model calculation are performed by shifting the bandhead spin by $2\hbar$ due to the core rotation contribution in the $\pi(g_{9/2})^{-2} \otimes \nu[h_{11/2}(g_{7/2})^3]$ configuration. For this configuration, the symmetric shears are formed between $j_\pi = 4.5\hbar$ and $j_\nu = 15\hbar$. For four neutron particles and two proton holes, $n = 8$. The shears parameters used were $j = 4.5\hbar$, $a = 3.33$, $V_{\pi\nu} = 1.2$ MeV and $V_{\pi\pi} = 0.15$ MeV. For the negative-parity band with the configuration under consideration, $I_{\rm sh}^{\rm max} = 24\hbar$, $I_{\rm max} = 25\hbar$, and $\Im = 2.67\,\hbar^2{\rm MeV}^{-1}$. The bandhead frequency is $\hbar\omega \approx 0.518$ MeV at $I = 17\hbar$. Similarly, $\Im_c$ was estimated to be $17\ \hbar^2{\rm MeV}^{-1}$ using the slope of the $I(\omega)$ plot [Fig. 6(b)] for the band before the neutron alignment. Both the $B(E2)$ and $I(\omega)$ plots for the $\pi g_{9/2}^{-2}$ based configuration with $2\hbar$ core contribution do not exhibit general agreement with the experimental values and considerable deviations are observed [Fig. 6(b)].

Secondly, for the $\pi(g_{9/2})^{-4} \otimes \nu[h_{11/2}(g_{7/2})^3]$ configuration, the symmetric shears are formed between $j_\pi = 6$ and $j_\nu = 13$. For four neutron particles and four proton holes, there are sixteen possible particle-hole pairs, which implies $n = 16$. The shears parameters used were $j = 6\hbar$, $a = 2.167$, $V_{\pi\nu} = 1.2$ MeV and $V_{\pi\pi} = 0.15$ MeV. The bandhead frequency is $\hbar\omega \approx 0.402$ MeV at $I = 17\hbar$. The other parameters used are $I_{\rm sh}^{\rm max} = 25\hbar$, $I_{\rm max} = 25\hbar$, and $\Im = 0\,\hbar^2{\rm MeV}^{-1}$. $\Im_c$ was estimated to be $17\ \hbar^2{\rm MeV}^{-1}$ using the slope of the $I(\omega)$ plot [Fig. 6(b)] for the band before the neutron alignment. Both the $B(E2)$ and $I(\omega)$ plots for the $\pi g_{9/2}^{-4}$ based configuration exhibit general agreement with the experimental values above $I \geqslant 17\hbar$.

In the previous work [17] a cranked Nilsson-Strutinsky formalism (CNS) was also shown to favor the $\pi(g_{9/2})^{-4} \otimes \nu[h_{11/2}(g_{7/2})^3]$ configuration for this negative-parity band. The calculations indicate this configuration terminating at $I = 25\hbar$ and also suggest that this band has been observed up to termination. The difference between this mechanism and AMR is reflected in the variation of the dynamic moment of inertia $\Im^{(2)}$ and $B(E2)$ strength as a function of spin. In the case of smoothly terminating bands, the ratio $\Im^{(2)}/B(E2)$ remains almost constant, in contrast to a sharp increase in the case of an AMR band. The sharp rise observed in the experimental values is characteristic of antimagnetic rotation, reflecting the fact that $\Im^{(2)}$ is essentially constant whereas the $B(E2)$ values rapidly approach zero as the spin increases along the band. The decreasing trends of the deduced quadrupole transition strength $B(E2)$ with spin, along with large $\Im^{(2)}/B(E2)$ values, conclusively establish the origin of these states as arising from antimagnetic rotation. Overall, the

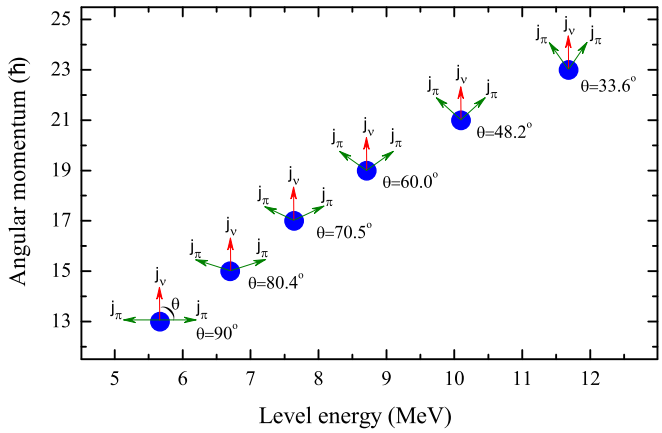

FIG. 7. A pictorial representation of the symmetric shears structure in ^{100}Pd. The higher spin states are generated by the gradual closing of the shears angle.

$\pi(g_{9/2})^{-4}$ based configuration of the symmetric shears with each of the proton blades consisting of two $\pi(g_{9/2})^{-2}$ holes is likely for this quadrupole cascade. It is worth noting that the shears angle (θ) is the only variable in the present model, and every angular momentum state corresponds to a unique θ, which is determined from Eq. (2). A pictorial representation of generation of the angular momentum by closing of the twin-shears structure over the observed spin range in ^{100}Pd is shown in Fig. 7.

V. CONCLUSIONS

The lifetimes of the states of the yrast negative-parity band of ^{100}Pd have been measured using the Doppler-shift attenuation method. The measured quadrupole transition rates exhibit a decreasing behavior with increasing angular momentum in the domain of $17\hbar \leqslant I \leqslant 21\hbar$. In addition, the observed $\Im^{(2)}/B(E2)$ values for these levels are large. The semiclassical particle-rotor model calculations favor the AMR phenomenon based on the $\pi(g_{9/2})^{-4} \otimes \nu[h_{11/2}\,(g_{7/2})^3]$ configuration and explain the experimental $B(E2)$ and $I(\omega)$ plots. Thus, it is concluded that the properties of the negative-parity band in ^{100}Pd are best described by a possible AMR band.

ACKNOWLEDGMENTS

The authors thank the TIFR-BARC Pelletron Linac Facility staff for providing a quality ion beam. The joint efforts of the members of INGA Collaboration for setting up the array are acknowledged. Financial support under the Centre of Advanced Study Funds, DST (FIST, Project No. SERB/F/4422/2016-17) and CSIR (Project No. 03/(1443)/18/EMR-II), New Delhi, is duly acknowledged.

[1] A. O. Macchiavelli, R. M. Clark, M. A. Deleplanque, R. M. Diamond, P. Fallon, I. Y. Lee, F. S. Stephens, and K. Vetter, Phys. Rev. C **58**, R621 (1998).
[2] R. M. Clark and A. O. Macchiavelli, Annu. Rev. Nucl. Part. Sci. **50**, 1 (2000).
[3] S. Frauendorf, Rev. Mod. Phys. **73**, 463 (2001).
[4] P. W. Zhao, J. Peng, H. Z. Liang, P. Ring, and J. Meng, Phys. Rev. Lett. **107**, 122501 (2011).
[5] A. J. Simons *et al.*, Phys. Rev. Lett. **91**, 162501 (2003).
[6] D. Choudhury *et al.*, Phys. Rev. C **82**, 061308(R) (2010).
[7] S. Roy and S. Chattopadhyay, Phys. Rev. C **87**, 059801 (2013).
[8] P. Datta *et al.*, Phys. Rev. C **71**, 041305(R) (2005).
[9] D. Choudhury *et al.*, Phys. Rev. C **87**, 034304 (2013).
[10] Santosh Roy *et al.*, Phys. Lett. B **694**, 322 (2011).
[11] V. Singh *et al.*, J. Phys. G **44**, 075105 (2017).
[12] N. Rather *et al.*, Phys. Rev. C **89**, 061303(R) (2014).
[13] S. Ali, S. Rajbanshi, B. Das, S. Chattopadhyay, M. SahaSarkar, A. Goswami, R. Raut, A. Bisoi, S. Nag, S. Saha, J. Sethi, R. Palit, G. Gangopadhyay, T. Bhattacharjee, S. Bhattacharyya, G. Mukherjee, A. K. Singh, and T. Trivedi, Phys. Rev. C **96**, 021304(R) (2017).
[14] S. Rajbanshi *et al.*, Phys. Lett. B **748**, 387 (2015).
[15] P. W. Zhao, J. Peng, H. Z. Liang, P. Ring, and J. Meng, Phys. Rev. C **85**, 054310 (2012).
[16] G. E. Perez *et al.*, Nucl. Phys. A **686**, 41 (2001).
[17] S. Zhu *et al.*, Phys. Rev. C **64**, 041302(R) (2001).
[18] J. C. Wells and N. R. Johnson, Oak Ridge National Laboratory Report No. ORNL-6689, 1991.
[19] R. Palit, Pramana J. Phys. **83**, 719 (2014).
[20] M. Kaur *et al.*, Proc. DAE-BRNS Symp. Nucl. Phys. **62**, 92 (2017).
[21] R. Palit *et al.*, Nucl. Instrum. Methods A **680**, 90 (2012).
[22] V. Singh *et al.*, Phys. Rev. C **95**, 064312 (2017).
[23] V. Singh *et al.*, Phys. Rev. C **94**, 044320 (2016).
[24] D. C. Radford, Nucl. Instrum. Methods A **361**, 306 (1995).
[25] A. Kramer-Flecken *et al.*, Nucl. Instrum. Methods A **275**, 333 (1989).
[26] K. Starosta *et al.*, Nucl. Instrum. Methods A **423**, 16 (1999).
[27] L. C. Northcliffe and R. F. Schilling, Nucl. Data Tables **A7**, 233 (1970).
[28] F. Brandolini and R. V. Ribas, Nucl. Instrum. Methods A **417**, 150 (1998).
[29] F. James and M. Roos, Comput. Phys. Commun. **10**, 343 (1975).
[30] A. O. Macchiavelli *et al.*, Phys. Lett. B **450**, 1 (1999).
[31] Santosh Roy and S. Chattopadhyay, Phys. Rev. C **83**, 024305 (2011).
[32] M. Sugawara *et al.*, Phys. Rev. C **79**, 064321 (2009).